CrossMark

# Globular Cluster UVIT Legacy Survey (GlobULeS). III. Omega Centauri in Far-ultraviolet

Deepthi S. Prabhu[1,2] , Annapurni Subramaniam[1] , Snehalata Sahu[3] , Chul Chung[4] , Nathan W. C. Leigh[5,6] ,
Emanuele Dalessandro[7] , Sourav Chatterjee[8] , N. Kameswara Rao[1] , Michael Shara[6] , Patrick Côté[9] ,
Samyaday Choudhury[10] , Gajendra Pandey[1] , Aldo A. R. Valcarce[11,12] , Gaurav Singh[1] , Joesph E. Postma[13] ,
Sharmila Rani[1] , Avrajit Bandyopadhyay[14] , Aaron M. Geller[15] , John Hutchings[9], Thomas Puzia[16] , Mirko Simunovic[17] ,
Young-Jong Sohn[4] , Sivarani Thirupathi[1] , and Ramakant Singh Yadav[18]
[1] Indian Institute of Astrophysics, Koramangala II Block, Bangalore-560034, India; deepthi.prabhu@iiap.res.in
[2] Pondicherry University, R.V. Nagar, Kalapet, 605014, Puducherry, India
[3] Department of Physics, University of Warwick, Coventry CV4 7AL, UK
[4] Department of Astronomy & Center for Galaxy Evolution Research, Yonsei University, Seoul 03722, Republic of Korea
[5] Departamento de Astronomía, Facultad Ciencias Físicas y Matematicas, Universidad de Concepción, Av. Esteban Iturra s/n Barrio Universitario, Casilla 160-C, Concepción, Chile
[6] Department of Astrophysics, American Museum of Natural History, Central Park West and 79th Street, New York, NY 10024-5192, USA
[7] INAF–Astrophysics and Space Science Observatory Bologna, Via Gobetti 93/3 I-40129 Bologna, Italy
[8] Tata Institute of Fundamental Research, Mumbai 400005, India
[9] Herzberg Astronomy and Astrophysics Research Centre, National Research Council of Canada, 5071 West Saanich Road, Victoria, BC V9E 2E7, Canada
[10] Space Telescope Science Institute, 3700 San Martin Drive, Baltimore, MD 21218, USA
[11] Departamento de Física, Universidade Estadual de Feira de Santana, Av. Transnordestina, s/n, 44036-900, Feira de Santana, BA, Brazil
[12] Millennium Institute of Astrophysics MAS, Nuncio Monsenor Sotero Sanz 100, Of. 104, Providencia, Santiago, Chile
[13] Department of Physics and Astronomy, University of Calgary, Calgary, AB T2N 1N4, Canada
[14] Department of Astronomy, University of Florida, Gainesville, FL 32601, USA
[15] Center for Interdisciplinary Exploration and Research in Astrophysics (CIERA) and Department of Physics and Astronomy, Northwestern University, 1800 Sherman Avenue, Evanston, IL 60201, USA
[16] Institute of Astrophysics, Pontificia Universidad Católica de Chile, Av. Vicuña MacKenna 4860, 7820436, Santiago, Chile
[17] Subaru Telescope, National Astronomical Observatory of Japan, 650 North Aohoku Place, Hilo, HI 96720, USA
[18] Aryabhatta Research Institute of Observational Sciences, Nainital, India

## Abstract

We present the first comprehensive study of the most massive globular cluster, Omega Centauri, in the far-ultraviolet (FUV), extending from the center to $\sim$28% of the tidal radius using the Ultraviolet Imaging Telescope on board AstroSat. A comparison of the FUV-optical color–magnitude diagrams with available canonical models reveals that horizontal branch (HB) stars bluer than the knee (hHBs) and the white dwarfs (WDs) are fainter in the FUV by $\sim$0.5 mag than model predictions. They are also fainter than their counterparts in M13, another massive cluster. We simulated HB with at least five subpopulations, including three He-rich populations with a substantial He enrichment of $Y$ up to 0.43 dex, to reproduce the observed FUV distribution. We find the He-rich younger subpopulations to be radially more segregated than the He-normal older ones, suggesting an in situ enrichment from older generations. The $\omega$ Cen hHBs span the same $T_{\rm eff}$ range as their M13 counterparts, but some have smaller radii and lower luminosities. This may suggest that a fraction of $\omega$ Cen hHBs are less massive than those of M13, similar to the result derived from earlier spectroscopic studies of outer extreme HB stars. The WDs in $\omega$ Cen and M13 have similar luminosity–radius–$T_{\rm eff}$ parameters, and 0.44–0.46 $M_\odot$ He-core WD model tracks evolving from progenitors with $Y = 0.4$ dex are found to fit the majority of these. This study provides constraints on the formation models of $\omega$ Cen based on the estimated range in age, [Fe/H], and $Y$ (in particular) for the HB stars.

## 1. Introduction

Galactic globular clusters (GCs) harbor stars hot enough to be significant emitters of ultraviolet (UV) light (see Moehler 2001, 2010, for detailed reviews). Studying these stars can help elucidate several problems in topics such as the late stages of low-mass stars' evolution (Moehler et al. 2019), stellar dynamics (e.g., Ferraro et al. 2012; Leigh et al. 2013), the "UV upturn" seen in the spectra of

elliptical galaxies (Greggio & Renzini 1990; Dorman et al. 1993, 1995), and so on. The identification of UV-bright stars is best done using UV images, as crowding due to populous cooler stars is suppressed in the central cores at these wavelengths.

Omega Centauri ($\omega$ Cen; or NGC 5139), being the most massive GC in the Galaxy (mass $= 3.5 \times 10^6\ M_\odot$; Baumgardt & Hilker 2018), contains the largest known population of very hot horizontal branch stars (HBs; D'Cruz et al. 2000) and exotic blue straggler stars (BSSs; Ferraro et al. 2006; Mucciarelli et al. 2014). Stars with a wide range in metallicity ($-2.2 \lesssim$ [Fe/H] $\lesssim -0.6$ dex) and helium (He) abundance ($Y$ up to 0.4 dex) have been reported through spectroscopic measurements (Moehler et al. 2011;

Moni Bidin et al. 2012; Latour et al. 2021, and references therein) and isochrone fitting and population synthesis of color–magnitude diagrams (CMDs; Norris 2004; Lee et al. 2005; Piotto et al. 2005; Joo & Lee 2013; Tailo et al. 2016). The presence of He-core white dwarfs (WDs) has also been suggested in the studies of Calamida et al. (2008) and Bellini et al. (2013).

The previous far-UV (FUV) study of this cluster was conducted decades back using the Ultraviolet Imaging Telescope (UIT; Landsman et al. 1992; Whitney et al. 1994, 1998) and the Hubble Space Telescope (HST; D'Cruz et al. 2000). However, these data sets are incomplete due to the limited spatial resolution of UIT ($\sim3'$) and field of view (FOV) of HST/WFPC2.

In this Letter, we present the first comprehensive FUV investigation of $\omega$ Cen extending from its center to $\sim28\%$ of the tidal radius, $r_t = 48'$ (Harris 1996, 2010 edition, hereafter H96), carried out using the Ultra Violet Imaging Telescope (UVIT) on board AstroSat. For the first time, we detect populations of HBs and WDs that are anomalously fainter in the FUV band as compared to theoretical models, as well as their counterparts in another massive GC, M13.

## 2. Observations and Data Reduction

Object $\omega$ Cen was observed as a part of the Globular Cluster UVIT Legacy Survey (GlobULeS; Sahu et al. 2022) on 2021 January 24 in two FUV filters, F148W and F169M, covering the entire $28'$ diameter FOV of the instrument. A detailed description of the UVIT and its calibration can be found in Tandon et al. (2017, 2020). The CCDLAB software package (Postma & Leahy 2017) was used to create the science-ready images with exposure times of 6310.95 s (F148W) and 6268.10 s (F169M). The astrometric calibration was performed using GALEX near-UV (NUV) imaging (Bianchi et al. 2017) and the Gaia EDR3 data (Gaia Collaboration et al. 2021) as references, and the final accuracy was $\sim0''.5$.

We performed point-spread function (PSF) photometry on these images as described in Sahu et al. (2022). The source catalog was refined by removing three visibly saturated stars and those lying at the edge of the UVIT FOV. The final catalog contains only the stars with PSF-fit errors less than 0.25 mag and those detected in both filters ($N = 3697$; obtained by matching the coordinates within a maximum match radius of $1''$). The UVIT image of the cluster in the F148W filter and the magnitude versus photometric error plots are shown in Figure 1.

The magnitudes were corrected for extinction by adopting $E(B - V)_{\mathrm{avg}} = 0.12$ mag (H96), $R_V = 3.1$, and the Fitzpatrick reddening law (Fitzpatrick 1999). The extinction coefficient values are 0.98 and 0.93 mag, respectively, for the F148W and F169M filters.[19]

## 3. Color–Magnitude Diagrams

The UV-optical CMD of the cluster was constructed by identifying the optical counterparts of the 3689 (out of a total of 3697) FUV-detected sources using the HST-based catalog of Bellini et al. (2017a; for $r <$ core radius $r_c = 2'.37$, hereafter inner region) and the catalogs of Stetson et al. (2019) and Vasiliev & Baumgardt (2021; for $2'.37 < r < 13'.5$ outer region) as described in Appendix A. The optical magnitudes were converted from the Vega to AB system using appropriate conversion factors.[20]
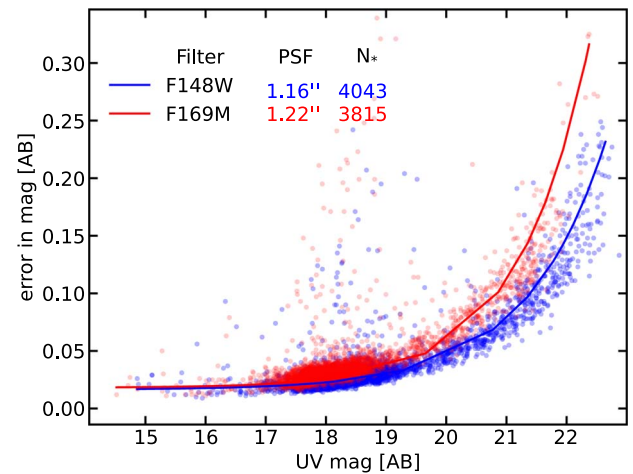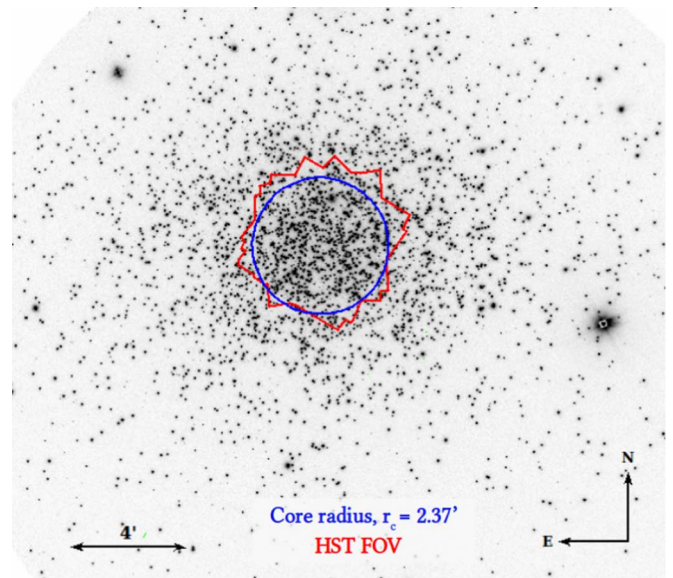




**Figure 1.** Top: UVIT/F148W image of $\omega$ Cen. Bottom: plot of PSF-fit errors vs. magnitude (not corrected for extinction) in the two filters. The filter names, FWHM of the PSF, and number of detections with fit error $<0.25$ mag ($N^*$) are indicated. The line indicates the median error in each filter.

Figure 2 shows the optical and FUV-optical CMDs of the cluster along with various models and isochrones. For the HB, we used the Bag of Stellar Tracks and Isochrones (BaSTI;[21] Pietrinferni et al. 2021) theoretical zero-age HB (ZAHB) and terminal-age HB (TAHB) models with $[\alpha/\mathrm{Fe}] = +0.4$ dex and mass-loss parameter $\eta = 0.3$, where overshooting is not applied and atomic diffusion effects are included. Three models with the following metallicity and He abundance values were chosen: [Fe/H] $= -2.2$, $Y = 0.247$ dex (metal-poor, He-normal); [Fe/H] $= -0.6$, $Y = 0.257$ dex (metal-intermediate, He-normal); and [Fe/H] $= 0.06$, $Y = 0.320$ dex (metal-rich, He-enhanced). These choices were based on the values reported in the literature and as per the availability in the database. For the BSS sequence, we used the BaSTI zero-age main-sequence (ZAMS) isochrone of age $= 0.5$ Gyr with an initial mass range of $\sim0.5$–$1.5\,M_\odot$ corresponding to [Fe/H]$_{\mathrm{avg}} = -1.55$ dex and a primordial $Y$ value. For the WD population, we used two DA spectral type models with a pure hydrogen (H) grid and thick H layers
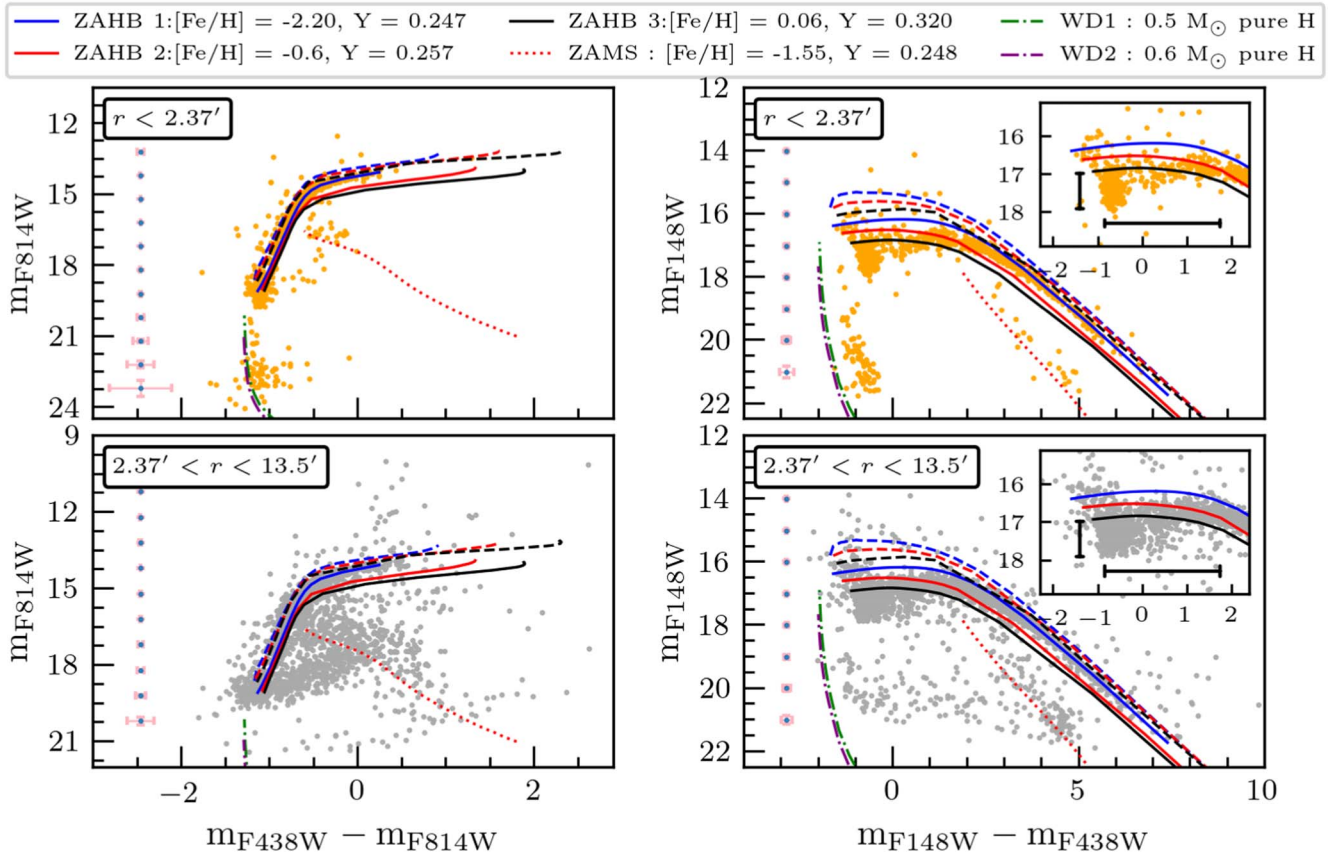
**Figure 2.** Theoretical stellar evolutionary models overplotted on the optical and FUV-optical CMDs. The BaSTI ZAHB and TAHB models for different metallicities and He abundances are shown with solid and dashed lines, respectively. The dotted lines represent the BaSTI ZAMS isochrone. The dashed–dotted lines represent WD cooling sequences. The parameters corresponding to all of the models are indicated in the top panel of the figure.

with masses of 0.5 and $0.6\,M_\odot$ (P. Bergeron 2022, private communication).

The locations of the HBs, BSSs, and WDs in the optical CMDs match well with the model predictions (left panels of Figure 2). In the FUV-optical CMDs (right panels), the red HB and BSS sequences lie at the locations expected from the models. It is well known that the hottest HBs, known as blue hook stars, appear fainter than canonical models in CMDs (Whitney et al. 1998; D'Cruz et al. 2000). However, we find that all hot HBs (hHBs) with $m_{F148W} - m_{F438W} \lesssim 2.0$ mag are fainter in the F148W band by about $\sim 0.5$ mag, whereas no anomaly is observed in optical CMDs. The WDs too are redder by comparable magnitude only in the FUV-optical CMDs (implying fainter FUV magnitudes). A similar behavior is observed in the UVIT F169M filter (not shown here). Any effect due to the instrument calibration or analysis procedure was ruled out as described in Appendix B.

## 4. HB Simulations

To check if the observed HB distribution originated from the extreme He enhancement, we produced the synthetic CMDs shown in the top and middle panels of Figure 3. Generally, the CMD synthesis of GCs should simultaneously reproduce both the HB morphology and the main sequence (MS) to red giant branch stars (RGBs). We can derive reliable stellar parameters and subpopulation ratios based on this. However, due to the observational limitations on the MS to RGBs in the FUV regime, we performed CMD synthesis only for HBs by referring to the stellar parameters of Joo & Lee (2013) for $\omega$ Cen, who reproduced both sequences

simultaneously. We adjusted three stellar parameters, $Y_{ini}$, age, and [Fe/H], to find the best match to the observations. The mass-loss parameter was adopted as $\eta = 0.5$ for all stellar populations. The detailed descriptions for other parameters and the simulation are summarized in Chung et al. (2017). Note that we did not include the evolved phase of HBs (i.e., the asymptotic giant branch-manqué phase; AGB-manqué) in the model to avoid the highly uncertain stellar evolution tracks after the He-core depletion.

We assumed five subpopulations to reproduce HB morphologies in two observed CMDs. From G1 to G5, the stellar parameters for each subpopulation are indicated above the top panel of Figure 3. The normal He G1 ($Y_{ini} = 0.23$) and slightly He-rich G2 ($Y_{ini} = 0.28$) show reasonable agreements with the observed blue HBs. In our simulation, the extremely hot HBs mainly originated from the G3 and G4 populations with $Y_{ini} = 0.43$ and 0.38, respectively. If we do not change $Y_{ini}$, other values of age or metallicity (i.e., extremely old or metal-poor populations) cannot reproduce those HBs. In addition, as Figure 6 of Joo & Lee (2013) shows, $\omega$ Cen hosts at least one extremely metal-rich MS-to-RGB sequence. To explain this population, we added the G5 population with [Fe/H] = $-0.4$ dex and $Y_{ini} = 0.38$ dex, and this subpopulation matches HBs around (F148W $-$ F438W) $\simeq 0.0$ as well. The fractions of the simulated subpopulations from G1 to G5, adopted based on Joo & Lee (2013), are 0.49, 0.27, 0.10, 0.07, and 0.07, respectively.

The FUV-optical CMD and the radial distribution of the HB stars belonging to different subpopulations are shown in the bottom panels of Figure 3. Here the older, He-normal subpopulations G1 and G2 were grouped together (purple symbols in the
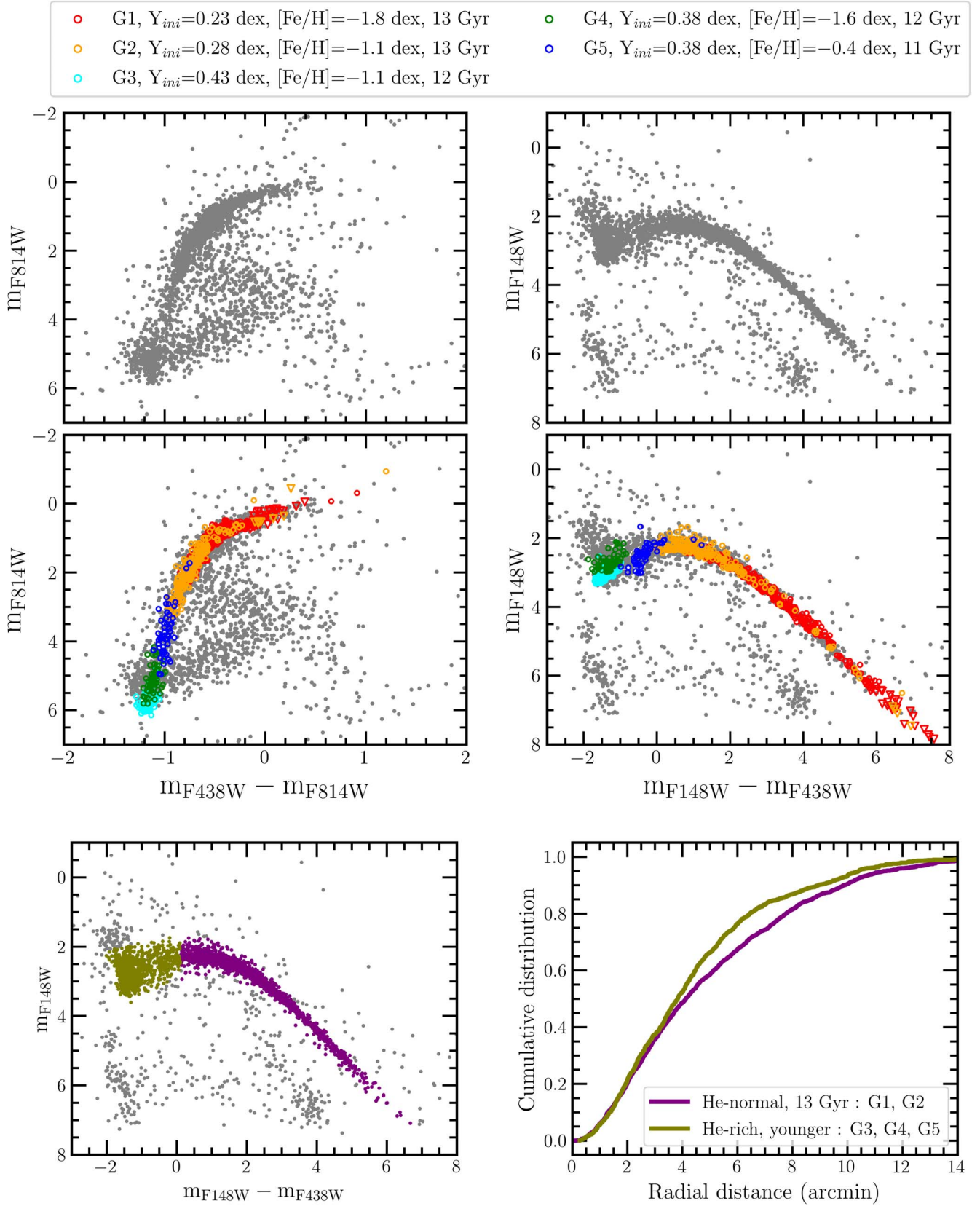
**Figure 3.** The HB simulations and radial distributions of subpopulations. The top panels show the observed optical and FUV-optical CMDs, and the middle panels show the simulated HB CMDs overplotted on the observed. Parameters suggested from our best-fit simulation for subpopulations from G1 to G5 are indicated in the legend above. The triangles in the middle panels denote the simulated RR Lyrae stars. The distance modulus and reddening adopted to reproduce the observed CMDs are $(m-M)_{F148W} = 15.5$, $E(F148W - F438W) = 1.2$ mag and $(m-M)_{F814W} = 14.1$, $E(F438W - F814W) = 0.3$ mag, respectively. The bottom right panel shows the radial distribution of observed HB subpopulations, where G1 and G2 are considered as a single group and G3, G4, and G5 as another, indicated with purple and olive symbols, respectively, in the bottom left panel.

bottom left panel) and the younger, He-rich G3, G4, and G5 were combined as another sample (olive symbols). The He-rich, second-generation HB stars clearly appear more segregated. The Kolmogorov–Smirnov test returned a $p$-value of $\sim 1 \times 10^{-5}$, indicating that the two subpopulations are not drawn from the same distribution.

## 5. Characterization of Hot Populations

We used the spectral energy distribution (SED) fitting technique to characterize the hot stars that showed a departure from the BaSTI tracks. The SEDs were constructed and fitted with appropriate models using the VO SED Analyser (VOSA; Bayo & Rodrigo 2008), which generates synthetic photometric points for the chosen filters. The best-fit parameters were estimated by comparing the observed data with synthetic photometry using a $\chi^2$ minimization method with $\chi^2_{\rm red}$ given by the relation

$$\chi^2_{\rm red} = \frac{1}{N - N_f} \sum_{i=1}^{N} \left\{ \frac{(F_{o,i} - M_d F_{m,i})^2}{\sigma^2_{o,i}} \right\}. \quad (1)$$

Here $N$ and $N_f$ are the numbers of observed data points and the model parameters fitted, respectively; $F_{o,i}$ is the observed flux; $F_{m,i}$ is the model flux; $M_d = \left(\frac{R}{D}\right)^2$ is the multiplicative dilution factor (where $R$ and $D$ are the radius and distance to the star, respectively); and $\sigma_{o,i}$ is the observed flux error. VOSA calculates two additional parameters, $Vgf$ and $Vgf_b$, as visual goodness-of-fit indicators, useful when the observational flux errors are underestimated.[22] We used $D_{\rm avg} = 5.426$ kpc (Baumgardt & Vasiliev 2021). To account for the extinction, VOSA uses the Fitzpatrick reddening relation. The errors in the fitted parameters were estimated using the statistical approach described in the VOSA documentation.

### 5.1. Hot HB Stars

The SEDs of hHBs were fitted using six appropriate models whose parameters and available ranges are tabulated in Table 1. We employed three approaches aiming to test different aspects. In the first approach, we fitted the SEDs by adopting the values listed in the last column of Table 1 and fixing the value of $A_V$ to 0.372 mag for $E(B - V)_{\rm avg} = 0.12$ mag. In the next approach, to check for the effects due to radiative levitation observed in HBs hotter than the Grundahl jump ($T_{\rm eff} \sim 11,500$ K; Grundahl et al. 1999), we allowed the metallicity parameter to vary up to the solar value, keeping $A_V$ and the other parameter ranges unchanged. The final approach was meant to check for the effect of differential reddening reported in the cluster (Calamida et al. 2005; Bellini et al. 2017b), wherein we included $A_V$ as a fit parameter with a range of 0.279–0.775 mag corresponding to $E(B - V) = 0.09$–0.25 mag, keeping all other parameter ranges as in the last column of Table 1.

The top left panel of Figure 4 shows the FUV-optical CMD highlighting the sample of hHBs analyzed. Among the inner region stars, we chose all 421 HBs bluer than the knee point in the CMD (at color $\sim 2.0$ mag), which are shown with red circles and denoted as OC hHB-I. For these stars, the UVIT photometry in two filters was combined with the photometric data in 18 HST WFC3/UVIS filters from Bellini et al. (2017a). Among the outer sources, we chose the 150 extreme HB (EHB; $T_{\rm eff} \gtrsim 20,000$ K) stars with confirmed cluster membership

---

**Table 1**
Models and Parameter Ranges Adopted to Fit the SEDs of hHBs and WDs

| Model | Parameter | Available Range | Adopted Range |
|---|---|---|---|
| | | hHBs | |
| Kurucz ODF-NEW/ NOVER[a] | $T_{\rm eff}$ | 3500–50,000 K | 10,000–50,000 K |
| | $\log g$ | 0–5 dex | 3–5 dex |
| | [Fe/H] | −4.0 to 0.5 dex | −2.5 to −0.5 dex |
| TMAP Grid 2[b] | $T_{\rm eff}$ | 20,000–150,000 K | 20,000–100,000 K |
| | $\log g$ | 4–9 dex | 4–5.5 dex |
| TMAP Grid 4[b] | $T_{\rm eff}$ | 20,000–150,000 K | 20,000–100,000 K |
| | $\log g$ | 4–9 dex | 4–5.5 dex |
| | H mass fraction | 0–1 | 0–1 |
| TMAP Tübingen[b] | $T_{\rm eff}$ | 30,000–1,000,000 K | 30,000–100,000 K |
| | $\log g$ | 3.8–9 dex | 3.8–5.5 dex |
| | H mass fraction | 0–1 | Full range |
| | He mass fraction | 0–1 | Full range |
| Pacheco et al. (2021) | $T_{\rm eff}$ | 10,000–65,000 K | Full range |
| | $\log g$ | 4.5–6.5 dex | 4.5–5.5 dex |
| | [Fe/H] | −1.5 to 0.0 dex | −1.5 dex |
| | log[He/H] | −4.98 to 3.62 | Full range |
| Husfeld et al. (1989) | $T_{\rm eff}$ | 35,000–80,000 K | Full range |
| | $\log g$ | 4.0–7.0 dex | 4.0–5.5 dex |
| | $Y_{\rm He}$ | 0.0–0.7 dex | Full range |
| | | WDs | |
| Koester[c] | $T_{\rm eff}$ | 5000–80,000 K | Full range |
| | $\log g$ | 6.5–9.5 dex | Full range |
| Levenhagen[d] | $T_{\rm eff}$ | 17,000–100,000 K | Full range |
| | $\log g$ | 7.0–9.5 dex | Full range |

**Notes.**
[a] $[\alpha/\rm Fe] = 0.4$ dex; Castelli & Kurucz (2003).
[b] Werner & Dreizler (1999); Rauch & Deetjen (2003); Werner et al. (2003).
[c] Koester (2010).
[d] Levenhagen et al. (2017).

---

obtained through a cross-match with the sample of Latour et al. (2018; shown with blue circles and denoted as OC EHB-O). The SEDs of these stars were constructed by complementing the UVIT photometry with the data in five optical filters from the catalog of Stetson et al. (2019). We thus derived the physical parameters for a total of 571 hHBs using the three approaches mentioned above. Since the results were found not to differ much, the discussions below are based on the first approach (also shown in the figure).

Good fits, with $Vgf_b < 15$ (Rebassa-Mansergas et al. 2021), were achieved for about 97% of the hHBs. The middle left panel of Figure 4 shows the Hertzsprung–Russell (H-R) diagram for these stars along with the same ZAHB models as in Figure 2, early and late hot flasher (EHF and LHF) models (Cassisi et al. 2003), and a $0.44 M_\odot$ He-core DA-type WD model with a $Y_{\rm ini} = 0.4$, $Z = 0.0005$ dex progenitor
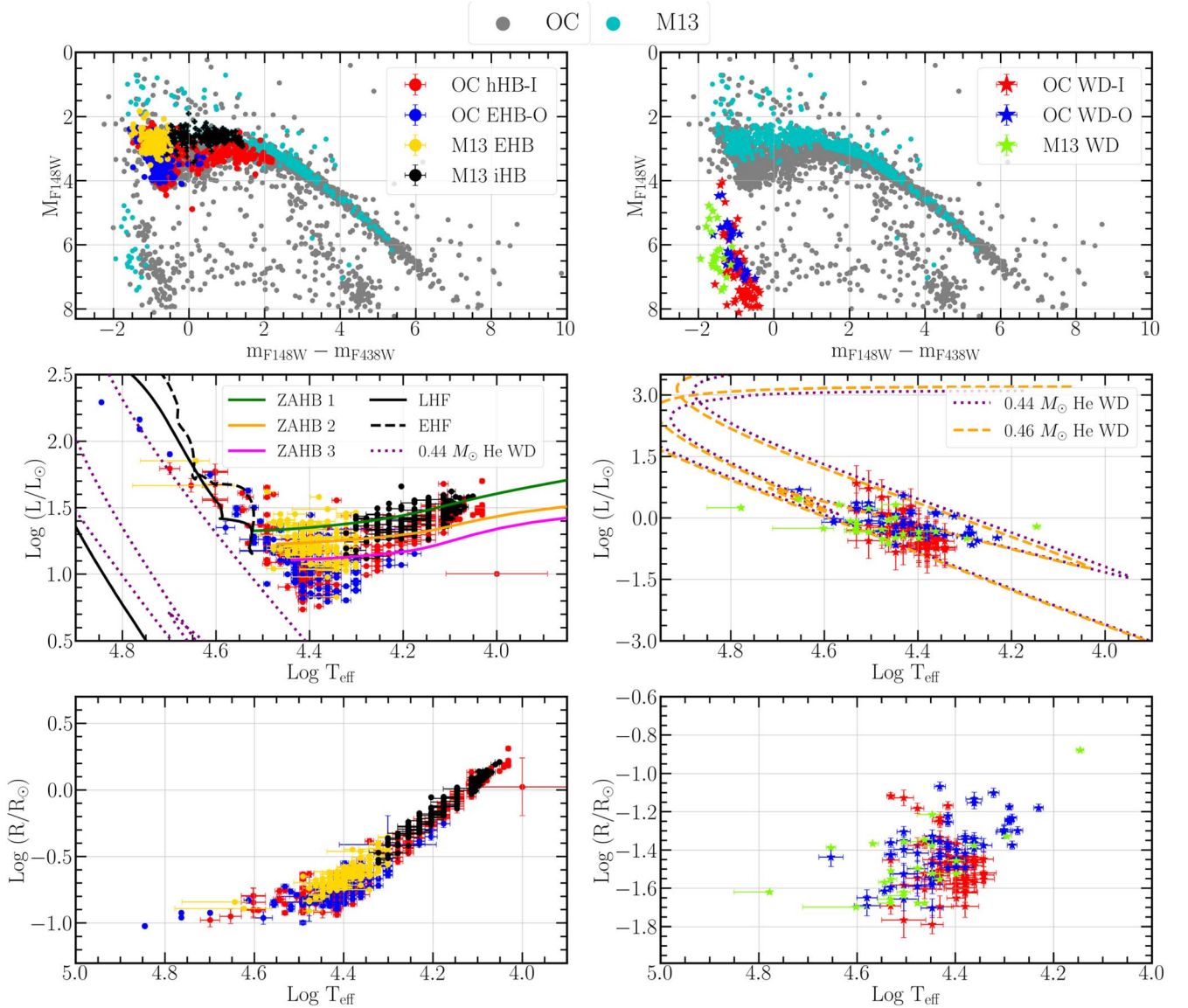
**Figure 4.** Comparison of the FUV-optical CMD, H-R diagram, and log $T_{eff}$ vs. log $(R/R_\odot)$ plots for $\omega$ Cen (OC) and M13 with a focus on the hHB population and WDs. The -I (-O) denotes stars within the inner (outer) region. The parameters corresponding to ZAHB models in the middle left panel are as follows: ZAHB 1, [Fe/H] = $-2.20$, $Y = 0.247$ dex; ZAHB 2, [Fe/H] = $-0.6$, $Y = 0.257$ dex; and ZAHB 3, [Fe/H] = $0.06$, $Y = 0.32$ dex. Here LHF has [M/H] = $-1.018$ dex, $Y = 0.250$ dex, and $M_{ZAHB} = 0.490\,M_\odot$, and EHF has [M/H] = $-1.90$ dex, $Y = 0.247$ dex, and $M_{ZAHB} = 0.502\,M_\odot$.

(Althaus et al. 2017). Most of the stars cooler than log $T_{eff} \sim$ 4.2 lie within the range of the ZAHB models. A significant fraction within log $T_{eff} \sim$ 4.2–4.5 are fainter than any of the ZAHB models. Their luminosity decreases with $T_{eff}$, reaching a minimum at log $T_{eff} \sim$ 4.4, which then increases further. The hHBs within log $T_{eff} \sim$ 4.5–4.65 are lying on the EHF and LHF tracks. The ones hotter than log $T_{eff} \sim$ 4.6 follow the 0.44 $M_\odot$ WD model. In the bottom left panel, the log $(R/R_\odot)$ of the hHBs are plotted as a function of the log $T_{eff}$, where the low-luminous hHBs of $\omega$ Cen are also found to be smaller in size.

### 5.2. WDs

The top right panel of Figure 4 shows the FUV-optical CMD highlighting the WD sample chosen for SED fitting. There are 77 (68) WD candidates from the inner (outer) region represented by red (blue) stars and denoted as OC WD-I (OC WD-O) whose SEDs were fitted using the models and parameters tabulated in Table 1. While inspecting the SEDs, we found about eight outer

WDs showing UV excess. Their SEDs could not be fit with single WD model and hence were not considered further. We also excluded the fits with $Vgf_b > 15$. The SED parameters for the rest of the sample (135 stars) are shown in the H-R diagram in the middle right panel of Figure 4, along with two He-core models of masses 0.44 and 0.46 $M_\odot$ with He-rich ($Y_{ini} = 0.4$ dex), $Z = 0.0005$ dex progenitors (Althaus et al. 2017).[23] Most stars lie in between the range of the models. The bottom right panel shows the (log $R/R_\odot$) of the WDs as a function of log $T_{eff}$, where the two populations of the WDs match well, except for a small number of cooler and larger WDs in the outer $\omega$ Cen.

## 6. Comparison of Hot Populations in $\omega$ Cen and M13

To further understand the peculiarities seen in the properties of hot stellar populations of $\omega$ Cen, we compared them with those of

---

[23] Note that the adopted He-core WD models do not result fromh binary evolution (see Althaus et al. 2017 for details).

another massive GC, M13 (or NGC 6205). Object M13 has [Fe/H] = −1.53 dex (H96), similar to the $\text{[Fe/H]}_{avg}$ of $\omega$ Cen with $\Delta Y_{max} \sim 0.05$ dex (Dalessandro et al. 2013; Milone et al. 2018) and age ≈13 Gyr (Denissenkov et al. 2017). Object M13 was also observed using UVIT as part of GlobULeS, and a detailed study has been carried out by Kumar et al. (2022). We obtained the final photometric data and the SED fit results of HBs (in the range $11,500\,\text{K} \leqslant T_{eff} \leqslant 30,000\,\text{K}$) and WDs from the authors. The intermediate-HBs (iHBs; $11,500\text{K} \leqslant T_{eff} \leqslant 20,000\,\text{K}$) are highlighted in black, the EHBs in yellow, and the WDs in light green symbols among the rest of the M13 FUV sources (cyan) on the FUV-optical CMDs (top panels of Figure 4). The $\omega$ Cen populations with $m_{F148W} - m_{F438W} \lesssim 2$ are clearly fainter in the FUV when compared to those of M13, whereas the locations of redder stars match well.

The $\omega$ Cen hHBs are, on average, less luminous than their counterparts in M13, and the latter also fall within the range of the ZAHB models as seen in the middle left panel. In the $\log T_{eff}$ versus $\log (R/R_\odot)$ plot, a few of the $\omega$ Cen hHBs (mostly near $\log T_{eff} \sim 4.4$) are found to have smaller radii than their M13 counterparts. This could explain their lower luminosities. The above may also imply that a fraction of hHBs in $\omega$ Cen are less massive than those of M13. The WDs in both clusters occupy similar positions in the H-R diagram and the $\log T_{eff}$ versus $\log (R/R_\odot)$ plot in the middle and bottom right panels, respectively.

## 7. Discussion and Summary

The first comprehensive FUV study of $\omega$ Cen reveals that HBs bluer than the knee point in the FUV-optical CMD and the WDs are fainter in the FUV by about $\sim$0.5 mag than canonical expectations and in comparison with populations of another cluster having similar properties, namely, M13. Moni Bidin et al. (2012), by deriving color–temperature relations, found analogous results uniquely for $\omega$ Cen hHBs in the $U$ band while detecting no anomaly in the $B$ and $V$ bands. The authors were unable to fully account for this.

We simulated the HB and compared it with observations to estimate He enhancements, metallicities, and ages of subpopulations. We find that at least five subpopulations with three He-rich ones are needed to explain the observed HB CMDs. As is well known, it would be challenging to determine metallicity and age using HB CMDs only. However, in terms of HB morphology, we conclude that a considerable amount of He enhancement is inevitable to explain the hHBs in FUV and optical CMDs. The fainter FUV magnitudes of hHBs could be due to the sensitivity of FUV bands to the $Y_{ini}$ range (Chung et al. 2017). A fraction of these FUV-faint hHBs could also be EHB stars with magnetic spots which are dark in the FUV bands, discovered by Momany et al. (2020). The derived parameters of the subpopulations are also comparable to the studies by Joo & Lee (2013). We find the He-rich younger subpopulations ($\sim$24%) to be radially more segregated than the He-normal older subpopulations ($\sim$76%), which is expected if the second-generation stars form from the ejecta of intermediate-mass AGBs (D'Ercole et al. 2008). Bellini et al. (2009) reported similar results for He-rich MS stars. The ranges in age, metallicity, and He content that are needed to fit the observed HB distribution provide constraints on the $\omega$ Cen formation models.

The properties of hHBs in $\omega$ Cen and M13 are generally comparable, except for a small fraction of low-luminous ones in $\omega$ Cen. Through spectroscopic measurements,

Moni Bidin et al. (2011) and Latour et al. (2018) reported a mean mass lower than canonical expectations for EHB stars in $\omega$ Cen (0.38 $M_\odot$) and could not explain this conundrum.

The WDs in $\omega$ Cen and M13 have similar physical parameters. However, unlike $\omega$ Cen, M13 is not known to host extreme He-rich stars that can form He-core WDs from single stellar evolution. Chen et al. (2021) suggested that the bright WDs in M13 are the result of slow cooling due to the residual hydrogen burning on the C/O WD surface. Hence, it is possible that some of the FUV-detected WDs in $\omega$ Cen are such slowly cooling C/O WDs. Photometric observations of WD pulsations in the future can shed more light in this direction (Althaus et al. 2017).

## Appendix A
## Cross-match of UVIT Detections with Different Catalogs

### A.1. UVIT–HST Cross-match

The optical counterparts of the FUV detections were identified by cross-matching those within the core radius of the cluster ($r_c = 2.'37$) with the HST data set from Bellini et al. (2017a). This astrophotometric data set was available in 18 WFC3/UVIS bands and eight WFC3/IR bands for 478,477 stars. However, we used only the WFC3/UVIS data, since the IR photometry did not include the information of the saturated stars, many of which belonged to the HB. The saturated stars also did not have proper-motion (PM) measurements in the catalog. Hence, we did not perform a filtering of the sources based on cluster membership. A direct cross-match of the UVIT and HST catalogs would result in many spurious identifications because of the differences in the spatial resolution and astrometric accuracy. Hence, we chose a subset of stars from the HST data set that included only the UV-bright stellar populations, such as HBs, post-HBs (pHBs), BSSs, and WDs. The HST photometry in Bellini et al. (2017a) was measured with three methods, each of which worked best in different magnitude regimes. Following the same selection criteria

as the authors, we used the results of method one photometry for HBs, pHBs, and BSSs and those of method two for WDs. The UV color–magnitude plane $m_{F275W} - m_{F336W}$ versus $m_{F275W}$ was used to select the HBs, pHBs, and BSSs, and the WDs were selected from the $m_{F438W} - m_{F606W}$ versus $m_{F438W}$ plane. This HST subset was cross-matched with the UVIT catalog with a maximum match radius of $0''\!.7$ using TOPCAT, and about 963 stars were found to have unique counterparts. We also manually verified that all of the cross-identifications were accurate. A counterpart could not be identified correctly for one star at R.A. $= 201\overset{\circ}{.}64700$ and decl. $= -47\overset{\circ}{.}50401$ in the UVIT catalog (it is not included in the HST catalog, although it is visible in the F555W image). So this star is excluded.

### A.2. UVIT Ground Data–Gaia EDR3 Cross-match

There were several UV-bright stars lying outside the HST FOV. In order to analyze these stars and plot them in the UV-optical CMD, we used the ground-based optical data set in the *UBVRI* filters from Stetson et al. (2019) and the Gaia EDR3 EDR3-based catalog from Vasiliev & Baumgardt (2021). The latter also included cluster membership probability estimates based on PM measurements. For the cross-match, we first created a subset of stars from the ground-based catalog, selecting only the population expected to be bright in UV. This subset was matched with the UVIT detections with a maximum cross-match radius of $0''\!.7$. The number of stars common in both was about 2725. In order to identify the cluster members among them, we matched this set further with the Gaia EDR3-based catalog of Vasiliev & Baumgardt (2021). About 1771 stars were found to have a membership probability of more than 0.5. However, there were about 803 UV-bright stars that were not included in the Gaia EDR3 catalog. Hence, their membership status is unknown. Finally, to plot all of the sources in a similar color–magnitude plane, we transformed the Johnson–Cousins *B*, *V*, and *I* magnitudes of the stars in the outer region into the corresponding HST WFC3/UVIS filters

(namely, F438W, F606W, and F814W) using the equations from Harris (2018).

### Appendix B
### Checks for Effects Due to Instrument Calibration or Analysis Procedure

We checked for various aspects that could possibly result in the bias observed in the FUV-optical CMDs. First, effects due to UVIT instrument-related aspects such as changes in calibration, sensitivity, and the slope of the transmission window were inspected. These were ruled out as magnitudes obtained from the recent observations of FUV-bright sources in the secondary calibration source, open cluster NGC 188, and a previously studied GC, NGC 2808, were consistent with earlier estimates. Next, we examined effects due to data reduction and analysis procedures. We obtained similar magnitudes (within $\sim 0.1$ mag) with science-ready images produced using CCDLAB and the official UVIT L2 pipeline, ruling out any issue due to the data reduction pipeline. Photometric analysis with IRAF was checked independently and found to be consistent. Lastly, we looked for possible changes introduced due to the transformation of optical magnitudes from the Vega to AB system. The bias was found even when the filter with the smallest transformation factor (F606W) was used, ruling out this possibility. In the top panels of Figure 5, we show the CMDs constructed using the UVIT F148W and HST F275W (NUV) and F336W (UV wide) filters, consisting of the 963 UVIT–HST common detections. We find that the hHBs and WDs show a deviation from model predictions in these CMDs also. Additionally, the CMD constructed using only the HST filters F275W and F336W with the data from Bellini et al. (2017a) also shows the deviation, supporting our analysis (bottom left panel of Figure 5). In the bottom right panel of Figure 5, we show the CMD with sources detected in both of the UVIT FUV filters.
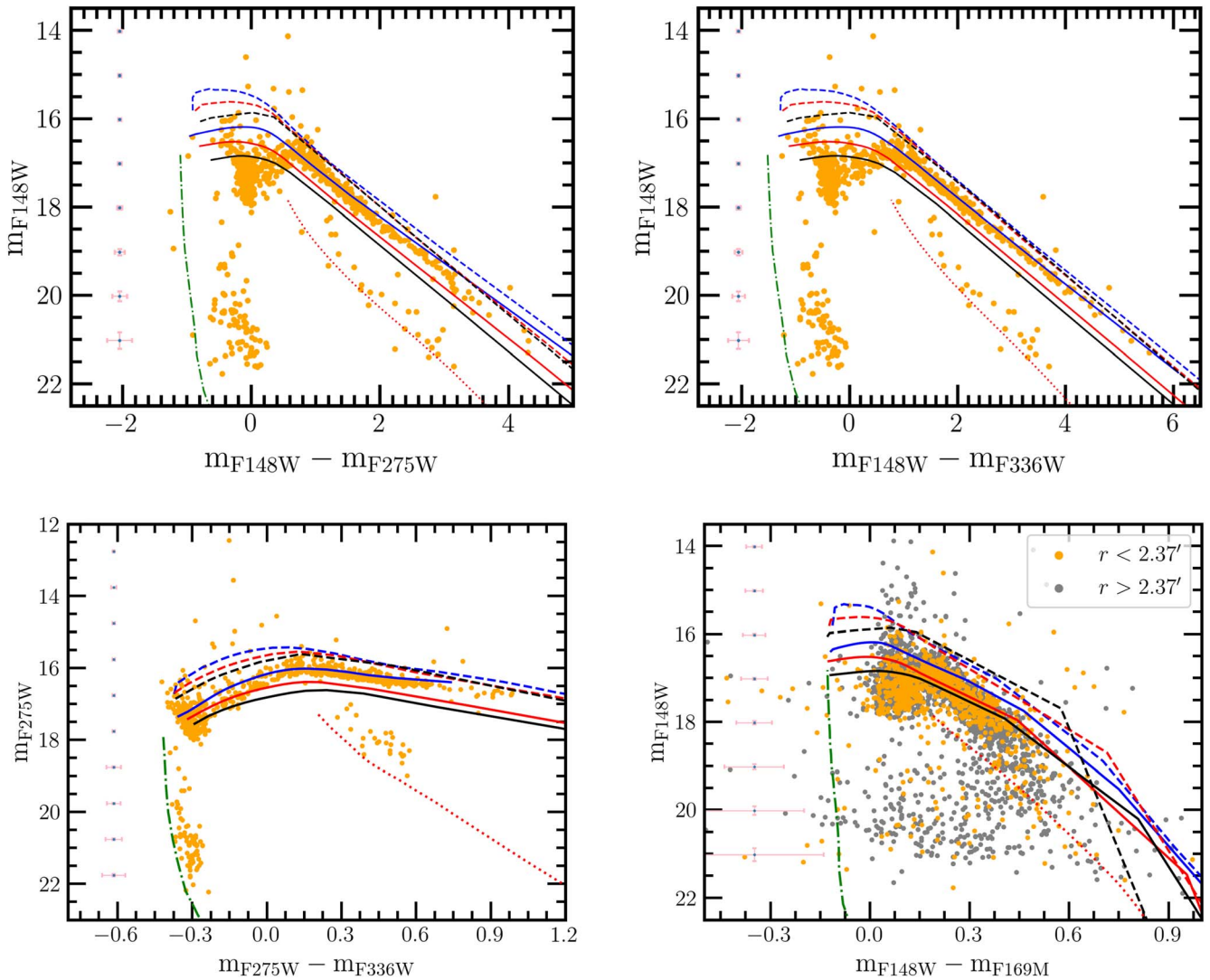
**Figure 5.** Top panels: UVIT/F148W−HST/F275W vs. HST/F275W and UVIT/F148W−HST/F336W vs. HST/F336W CMDs showing the UVIT–HST common detections (963 stars), along with the theoretical stellar evolutionary models shown in Figure 2. Bottom left: F275W−F336W vs. F275W CMD with the same 963 stars as above. Bottom right: CMD consisting of all of the sources detected in both the UVIT F148W and F169M filters, along with evolutionary models.

## ORCID iDs

Deepthi S. Prabhu ⓘ https://orcid.org/0000-0002-8217-5626
Annapurni Subramaniam ⓘ https://orcid.org/0000-0003-4612-620X
Snehalata Sahu ⓘ https://orcid.org/0000-0002-0801-8745
Chul Chung ⓘ https://orcid.org/0000-0001-6812-4542
Nathan W. C. Leigh ⓘ https://orcid.org/0000-0003-0347-276X
Emanuele Dalessandro ⓘ https://orcid.org/0000-0003-4237-4601
Sourav Chatterjee ⓘ https://orcid.org/0000-0002-3680-2684
N. Kameswara Rao ⓘ https://orcid.org/0000-0002-8414-8541
Michael Shara ⓘ https://orcid.org/0000-0003-0155-2539
Patrick Côté ⓘ https://orcid.org/0000-0003-1184-8114
Samyaday Choudhury ⓘ https://orcid.org/0000-0001-8182-9790
Gajendra Pandey ⓘ https://orcid.org/0000-0001-5812-1516
Aldo A. R. Valcarce ⓘ https://orcid.org/0000-0003-4623-3961
Gaurav Singh ⓘ https://orcid.org/0000-0003-2952-3617
Joesph E. Postma ⓘ https://orcid.org/0000-0002-3025-1412
Sharmila Rani ⓘ https://orcid.org/0000-0003-4233-3180
Avrajit Bandyopadhyay ⓘ https://orcid.org/0000-0002-8304-5444
Aaron M. Geller ⓘ https://orcid.org/0000-0002-3881-9332
Thomas Puzia ⓘ https://orcid.org/0000-0003-0350-7061

Mirko Simunovic ⓘ https://orcid.org/0000-0002-5652-6525
Young-Jong Sohn ⓘ https://orcid.org/0000-0003-4079-9534
Sivarani Thirupathi ⓘ https://orcid.org/0000-0003-0891-8994

## References

Althaus, L. G., De Geronimo, F., Corsico, A., Torres, S., & Garcia-Berro, E. 2017, A&A, 597, A67
Baumgardt, H., & Hilker, M. 2018, MNRAS, 478, 1520
Baumgardt, H., & Vasiliev, E. 2021, MNRAS, 505, 5957
Bayo, A., Rodrigo, C., Barrado Y Navascués, D., et al. 2008, A&A, 492, 277
Bellini, A., Anderson, J., Bedin, L. R., et al. 2017a, ApJ, 842, 6
Bellini, A., Anderson, J., Salaris, M., et al. 2013, ApJL, 769, L32
Bellini, A., Anderson, J., van der Marel, R. P., et al. 2017b, ApJ, 842, 7
Bellini, A., Piotto, G., Bedin, L. R., et al. 2009, A&A, 507, 1393
Bianchi, L., Shiao, B., & Thilker, D. 2017, ApJS, 230, 24
Calamida, A., Corsi, C. E., Bono, G., et al. 2008, ApJL, 673, L29
Calamida, A., Stetson, P. B., Bono, G., et al. 2005, ApJL, 634, L69
Cassisi, S., Salaris, M., & Irwin, A. W. 2003, ApJ, 588, 862
Castelli, F., & Kurucz, R. L. 2003, in IAU Symp. 210, Modelling of Stellar Atmospheres, ed. N. Piskunov, W. W. Weiss, & D. F. Gray (San Francisco, CA: ASP), A20
Chen, J., Ferraro, F. R., Cadelano, M., et al. 2021, NatAs, 5, 1170
Chung, C., Yoon, S.-J., & Lee, Y.-W. 2017, ApJ, 842, 91

Dalessandro, E., Salaris, M., Ferraro, F. R., Mucciarelli, A., & Cassisi, S. 2013, MNRAS, 430, 459
D'Cruz, N. L., O'Connell, R. W., Rood, R. T., et al. 2000, ApJ, 530, 352
Denissenkov, P. A., VandenBerg, D. A., Kopacki, G., & Ferguson, J. W. 2017, ApJ, 849, 159
D'Ercole, A., Vesperini, E., D'Antona, F., McMillan, S. L. W., & Recchi, S. 2008, MNRAS, 391, 825
Dorman, B., O'Connell, R. W., & Rood, R. T. 1995, ApJ, 442, 105
Dorman, B., Rood, R. T., & O'Connell, R. W. 1993, ApJ, 419, 596
Ferraro, F. R., Lanzoni, B., Dalessandro, E., et al. 2012, Natur, 492, 393
Ferraro, F. R., Sollima, A., Rood, R. T., et al. 2006, ApJ, 638, 433
Fitzpatrick, E. L. 1999, PASP, 111, 63
Gaia Collaboration, Brown, A. G. A., Vallenari, A., et al. 2021, A&A, 649, A1
Greggio, L., & Renzini, A. 1990, ApJ, 364, 35
Grundahl, F., Catelan, M., Landsman, W. B., Stetson, P. B., & Andersen, M. I. 1999, ApJ, 524, 242
Harris, W. E. 1996, AJ, 112, 1487
Harris, W. E. 2018, AJ, 156, 296
Husfeld, D., Butler, K., Heber, U., & Drilling, J. S. 1989, A&A, 222, 150
Joo, S.-J., & Lee, Y.-W. 2013, ApJ, 762, 36
Koester, D. 2010, MmSAI, 81, 921
Landsman, W. B., O'Connell, R. W., Whitney, J. H., et al. 1992, ApJL, 395, L21
Kumar, R., Pradhan, A., Sahu, S., et al. 2022, MNRAS, submitted
Latour, M., Calamida, A., Husser, T. O., et al. 2021, A&A, 653, L8
Latour, M., Randall, S. K., Calamida, A., Geier, S., & Moehler, S. 2018, A&A, 618, A15
Lee, Y.-W., Joo, S.-J., Han, S.-I., et al. 2005, ApJL, 621, L57
Leigh, N., Knigge, C., Sills, A., et al. 2013, MNRAS, 428, 897
Levenhagen, R. S., Diaz, M. P., Coelho, P. R. T., & Hubeny, I. 2017, ApJS, 231, 1
McCall, M. L. 2004, AJ, 128, 2144
Milone, A. P., Marino, A. F., Renzini, A., et al. 2018, MNRAS, 481, 5098
Moehler, S. 2001, PASP, 113, 1162
Moehler, S. 2010, MmSAI, 81, 838
Moehler, S., Dreizler, S., Lanz, T., et al. 2011, A&A, 526, A136
Moehler, S., Landsman, W. B., Lanz, T., & Miller Bertolami, M. M. 2019, A&A, 627, A34
Momany, Y., Zaggia, S., Montalto, M., et al. 2020, NatAs, 4, 1092
Moni Bidin, C., Villanova, S., Piotto, G., Moehler, S., & D'Antona, F. 2011, ApJL, 738, L10
Moni Bidin, C., Villanova, S., Piotto, G., et al. 2012, A&A, 547, A109
Mucciarelli, A., Lovisi, L., Ferraro, F. R., et al. 2014, ApJ, 797, 43
Norris, J. E. 2004, ApJL, 612, L25
Pacheco, T. A., Diaz, M. P., Levenhagen, R. S., & Coelho, P. R. T. 2021, ApJS, 256, 41
Pietrinferni, A., Hidalgo, S., Cassisi, S., et al. 2021, ApJ, 908, 102
Piotto, G., Villanova, S., Bedin, L. R., et al. 2005, ApJ, 621, 777
Postma, J. E., & Leahy, D. 2017, PASP, 129, 115002
Rauch, T., & Deetjen, J. 2003, in ASP Conf. Ser. 288, Stellar Atmosphere Modeling, ed. I. Hubeny, D. Mihalas, & K. Werner (San Francisco, CA: ASP), 103
Rebassa-Mansergas, A., Solano, E., Jimenez-Esteban, F. M., et al. 2021, MNRAS, 506, 5201
Sahu, S., Subramaniam, A., Singh, G., et al. 2022, MNRAS, 514, 1122
Stetson, P. B., Pancino, E., Zocchi, A., Sanna, N., & Monelli, M. 2019, MNRAS, 485, 3042
Tailo, M., Di Criscienzo, M., D'Antona, F., Caloi, V., & Ventura, P. 2016, MNRAS, 457, 4525
Tandon, S. N., Postma, J., Joseph, P., et al. 2020, AJ, 159, 158
Tandon, S. N., Subramaniam, A., Girish, V., et al. 2017, AJ, 154, 128
Vasiliev, E., & Baumgardt, H. 2021, MNRAS, 505, 5978
Werner, K., Deetjen, J. L., Dreizler, S., et al. 2003, in ASP Conf. Ser. 288, Stellar Atmosphere Modeling, ed. I. Hubeny, D. Mihalas, & K. Werner (San Francisco, CA: ASP), 31
Werner, K., & Dreizler, S. 1999, JCoAM, 109, 65
Whitney, J. H., O'Connell, R. W., Rood, R. T., et al. 1994, AJ, 108, 1350
Whitney, J. H., Rood, R. T., O'Connell, R. W., et al. 1998, ApJ, 495, 284